Chemical Science

ROYAL SOCIETY OF CHEMISTRY

EDGE ARTICLE

View Article Online
View Journal | View Issue

Cite this: *Chem. Sci.*, 2026, **17**, 6972

All publication charges for this article have been paid for by the Royal Society of Chemistry

Single-B/N MR-TADF emitters enhancing electroluminescence efficiency *via* a "terminal engineering" strategy

Hengxuan Qi,†[abc] Hao Liu,†[d] Deli Li,†[e] Lin Wu,*[bc] Jiasen Zhang,[bc] Huaxin Li,[bc] Ziru Xin,[bc] Chao Xia,[bc] Ruixiang Peng,*[bc] Wenjun Wang,[a] Zujin Zhao,*[d] Wei Li*[bc] and Ziyi Ge*[bc]

We implemented a "terminal engineering" strategy to address the challenges of low efficiency and the difficulty of effectively narrowing the emission spectra within the single boron–nitrogen (BN) multi-resonance thermally activated delayed fluorescence (MR-TADF) emitter system. By adding flexible diphenylamino groups and insulating *tert*-butyl (*t*-Bu) groups, respectively, into the structurally simple CzBN and the polycyclic aromatic hydrocarbon (PAH)-based Indo-CzBN, two novel proof-of-concept MR-TADF emitters, DPA-CzBN and Indo-*t*CzBN, were successfully developed. Notably, the incorporation of *t*-butyl units into polycyclic aromatic hydrocarbon (PAH)-structured indolocarbazole derivatives not only markedly suppresses the vibration relaxation of the excited state, enabling Indo-*t*CzBN to achieve an exceptionally narrow full width at half maximum (FWHM) of 19 nm and a high photoluminescence quantum yield (PLQY) of up to 97.5%, but also significantly enhances the horizontal dipole orientation factor (Θ//) of Indo-*t*CzBN to 85.3%, compared to approximately 73.6% for Indo-CzBN. Accordingly, benefiting from the synergistic effect of a high Θ// factor and a high PLQY, both the non-sensitized and sensitized organic light-emitting diodes (OLEDs) based on Indo-*t*CzBN achieved maximum external quantum efficiencies (EQE_{max}) of 37.4% and 39.0%, respectively. These values rank among the highest reported for MR-TADF emitters constructed on a single BN molecular architecture.

Received 23rd December 2025
Accepted 9th February 2026

DOI: 10.1039/d5sc10069k

rsc.li/chemical-science

Introduction

With the rapid development of display technology, organic light-emitting diodes (OLEDs) have become one of the most promising options for next-generation displays, owing to their numerous advantages, including low power consumption, high color purity, wide viewing angles, fast response times, and affordability. They show particular promise in demanding applications such as virtual reality (VR), augmented reality (AR), and ultra-high-definition displays with resolutions of 8K and above.[1] Therefore, developing new high-performance electroluminescent (EL) materials and improving OLED performance across efficiency, lifetime, and color quality has become a critical issue requiring urgent attention.[2] Color purity is generally measured by the full width at half maximum (FWHM) of the luminescent materials. However, traditional fluorescent materials tend to have relatively broad emission spectra due to vibrational coupling from local excited (LE) states.[3] Meanwhile, phosphorescent materials containing heavy atoms usually exhibit broad emission bands due to ligand-to-ligand charge-transfer (LLCT) and metal-to-ligand charge-transfer (MLCT) processes.[4] As a result, both types struggle to achieve high color purity. Thanks to the innovative work of researcher Hatakeyama, who cleverly embedded boron (B) atoms alongside electron-donating heteroatoms such as N, O, S, and Se within a rigid polycyclic aromatic hydrocarbon (PAH) framework, successfully inducing multiple resonance (MR) effects.[5] He later developed a new type of narrow-band luminescent material, known as MR thermally activated delayed fluorescence (MR-TADF).[5a] The emergence of these materials has driven continuous progress in OLED technology over the past decade, with hundreds of highly efficient MR-TADF emitters reported.[2c–e]

More importantly, numerous factors influence the performance of EL materials in OLEDs. Among these, the most

[a]*School of Physical Science and Information Technology, Liaocheng University, Liaocheng 2520259, P. R. China*

[b]*Zhejiang Provincial Engineering Research Center of Energy Optoelectronic Materials and Devices, Ningbo Institute of Materials Technology and Engineering, Chinese Academy of Sciences, Ningbo, 315201, P. R. China. E-mail: pengrx@nimte.ac.cn; liwei1987@nimte.ac.cn; geziyi@nimte.ac.cn*

[c]*Center of Materials Science and Optoelectronics Engineering, University of Chinese Academy of Sciences, P. R. China*

[d]*State Key Laboratory of Luminescent Materials and Devices and Institute of South China University of Technology, Wushan Road 381, Tianhe District, Guangzhou 510640, Guangdong Province, P. R. China. E-mail: mszjzhao@scut.edu.cn*

[e]*Institute for Smart Materials & Engineering, University of Jinan, No. 336 Nanxinzhuang West Road, Jinan, 250022, P. R. China*

† These authors contributed equally to this work.

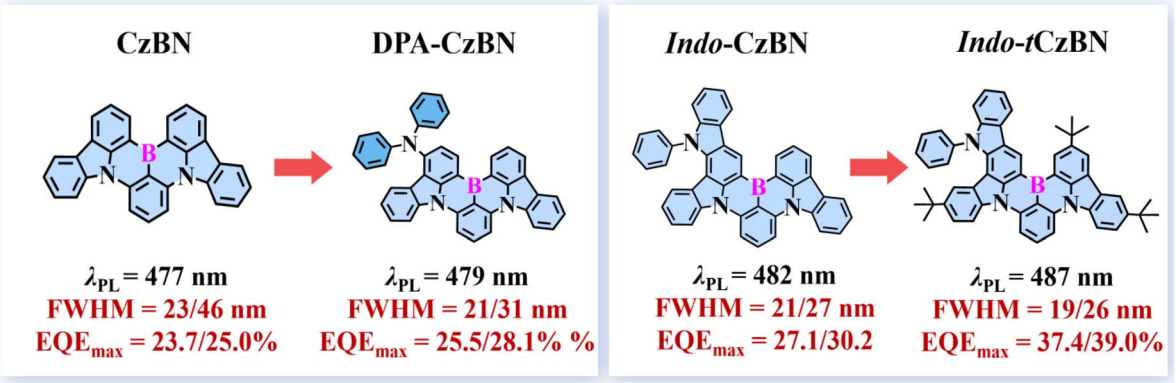

Scheme 1 . Molecular design strategy and chemical structures of DPA-CzBN, Indo-CzBN, and Indo-*t*CzBN. Herein, the FWHM values correspond to data from dilute toluene solution and from non-sensitized OLEDs at a 3 wt% doping concentration. The EQE values are derived from the non-sensitized system and the interlayer HF-OLEDs.

significant is the photoluminescence quantum yield (PLQY) of the emitters under photoluminescence (PL) conditions, as it primarily determines their potential for EL efficiency.[6] Fortunately, MR-TADF emitters are typically constructed on a highly rigid polycyclic aromatic hydrocarbon (PAH) framework, which inherently suppresses non-radiative transition processes, thereby facilitating high PLQY. Additionally, with respect to the exciton utilization ratio (EUR), MR-TADF materials generally exhibit a larger energy gap between the singlet (S_1) and triplet (T_1) states (ΔE_{ST}), resulting in longer delayed fluorescence lifetimes (τ_{DF}).[5b] However, this characteristic may impede T_1 excitons from reverting to the S_1 state *via* reverse intersystem crossing (RISC) and from attaining efficient electroluminescence *via* radiative decay, thereby limiting the full utilization of excitons. Two common strategies can be used to address the issues above. One method involves adding heavy atoms, such as Se, to exploit the heavy-atom effect and enhance spin–orbit coupling (SOC).[7] This boosts the RISC rate (κ_{RISC}) and enables faster upconversion and higher T_1 exciton yields. However, this approach may result in reduced thermal stability, broader emission spectra, and higher manufacturing costs, as forming Se-containing groups is often challenging. Another strategy involves adding inert or non-inert shielding groups into the molecular structure to improve the material's tolerance to doping levels. For example, Yang *et al.* achieved this by incorporating the 1,3-di(9*H*-carbazol-9-yl)benzene (mCP) group at the ortho position of the boron atom in the CzBN molecule.[8] Our team has also introduced 9,9′-spirobi[fluorene] (SF) or 1′,2′,3′,3a′,4′,5′,6′,6a′-octahydrospiro[fluorene-9,7′-[2,5]methanopentalene] groups onto the B/N-PAH framework to produce a similar effect.[9] However, this approach, while enabling the tuning of the emission wavelength, often complicates synthesis and can sometimes increase the FWHM values of the target molecules. Notably, in addition to the influence of the factors mentioned above on the EL performance of MR-TADF emitters, the effect of the aggregation morphology of organic molecules on device performance should not be overlooked. Generally, the external quantum efficiency (η_{out}) of bottom-OLEDs without additional light-extraction enhancement structures is ~20–30%. Studies have demonstrated that some luminescent materials exhibit pronounced anisotropy in device environments, with their transition dipole moments (TDMs) aligning parallel to the substrate plane. This highly ordered dipole orientation can effectively enhance optical outcoupling efficiency, thereby substantially improving overall EL performance.[10] Therefore, understanding the various factors influencing EL performance and developing effective EL materials using simple, practical experimental methods is a research area of both scientific and practical importance.

To address the issues above, we propose a "terminal engineering" strategy to simultaneously enhance EL efficiency and reduce the FWHM of the emission spectra. By introducing flexible diphenylamino (DPA) groups and insulating *tert*-butyl (*t*-Bu) groups, respectively, into the structurally simple CzBN and the polycyclic aromatic hydrocarbon (PAH)-based Indo-CzBN, two novel proof-of-concept MR-TADF emitters, DPA-CzBN and Indo-*t*CzBN, were successfully developed (Scheme 1). DPA was chosen for its electron-donating ability and conformational flexibility, which can modulate HOMO delocalization. *t*-Bu was selected for its steric bulk and insulating properties, which help suppress intermolecular quenching and enhance film morphology. It has been found that introducing DPA can only limit the reduction in the FWHM values of DPA-CzBN. However, indolocarbazole derivatives with a polycyclic aromatic hydrocarbon (PAH) structure can significantly inhibit vibration relaxation in the excited state, thereby considerably reducing the FWHM values of Indo-CzBN and Indo-*t*CzBN. As a result, the FWHM decreased from 23 nm for CzBN to 19 nm for Indo-*t*CzBN in dilute toluene solutions. Furthermore, based on the energy-loss mechanism driven by bimolecular electron–exchange interaction, which is dominated by short-range Dexter energy transfer (DET) in MR-TADF emitters, introducing insulating *t*-Bu can increase the intermolecular luminescent-center spacing, thereby effectively suppressing non-radiative energy loss and significantly enhancing their optoelectrical performance. Compared to CzBN (PLQY ~80.2%) and Indo-CzBN (PLQY ~85.7%), the PLQY of Indo-*t*CzBN with a *t*-Bu group has significantly increased to 97.5%. The PLQY is an average of

three measurements with a standard deviation of ±1.2%. Interestingly, adding insulating *t*-Bu significantly improves the horizontal dipole orientation (*Θ*//) factor of Indo-*t*CzBN (85.3%) compared to Indo-CzBN (~73.6%), thereby enhancing the EL performance of Indo-*t*CzBN. Accordingly, benefiting from the synergistic effect of a high *Θ*// factor and a high PLQY, the non-sensitized and sensitized OLEDs based on Indo-*t*CzBN achieved maximum external quantum efficiencies (EQE_{max}) of 37.4% and 39.0%, respectively, which rank among the highest reported for MR-TADF emitters built on a single BN molecular architecture. We believe this work opens up new avenues for exploration and offers promising luminescent materials suitable for ultra-high-definition (UHD) display applications, combining high efficiency with low manufacturing cost.

Results and discussion

DPA-CzBN and Indo-*t*CzBN were successfully designed and synthesized *via* a one-step boronization strategy with high yields (Scheme S1). CzBN and Indo-CzBN were also successfully synthesized using the same synthetic method for comparison. The synthetic route is shown in Scheme S1 and involves a one-step boronation reaction. All target compounds were systematically characterized by high-resolution mass spectrometry (HRMS), ^{1}H nuclear magnetic resonance (^{1}H NMR), and single-crystal X-ray diffraction to unambiguously confirm their molecular structures. The thermal decomposition temperatures (T_d, defined as the temperature at which 5% of the material's mass is lost) of DPA-CzBN, Indo-CzBN, and Indo-*t*CzBN reach as high as 492–530 °C, all surpassing that of the CzBN at 450 °C (Fig. S1). None of the molecules was detected to have a glass transition temperature (T_g), indicating that they are amorphous (Fig. S2). Therefore, OLEDs based on these emitters can be fabricated *via* vacuum evaporation technology due to their excellent thermal stability.

First, the electronic properties of four molecules in their ground (S_0) state were systematically investigated using density functional theory (DFT) (Fig. 1). It is worth noting that, based on the highest occupied molecular orbital (HOMO) distribution, the MR effects of the B/N units within the molecule cause all molecules to display significant non-bonding characteristics. This significantly weakens the coupling during the S_1-to-S_0 transition, resulting in a highly narrow emission spectrum. In particular, the HOMO distribution of CzBN and DPA-CzBN extends across the entire molecular framework. Because DPA-CzBN exhibits stronger HOMO delocalization than CzBN, its HOMO energy level is significantly shallower. In contrast, the HOMO energy levels of Indo-CzBN and Indo-*t*CzBN are deeper than that of DPA-CzBN because of the larger dihedral angles between the benzene ring and the molecular backbone (59.8° for Indo-CzBN and 59.3° for Indo-*t*CzBN), which restrict effective delocalization of the HOMO. Additionally, due to the hyperconjugation electron-donating effect of the *tert*-butyl carbazole group, the HOMO energy level of Indo-*t*CzBN is further shifted downward (*i.e.*, deeper) compared to Indo-CzBN. Given the planar structure of CzBN, its lowest unoccupied molecular orbital (LUMO) distribution extends across the entire molecule. DPA-CzBN also exhibits a LUMO distribution similar to that of CzBN, thereby achieving a LUMO energy level comparable to that of CzBN. The closed-loop structure enhances conjugation for Indo-CzBN and Indo-*t*CzBN. As a result, their LUMO energy levels extend to the parts of 12-phenyl-5,12-dihydroindolo[3,2-*a*]carbazole (Indo-Cz) and 2-(*tert*-butyl)-12-phenyl-5,12-dihydroindolo[3,2-*a*]carbazole (Indo-*t*Cz), leading to shallower LUMO energy levels compared to CzBN and DPA-CzBN (Fig. 1). It is worth noting that in Indo-*t*CzBN, the insulated *t*-Bu

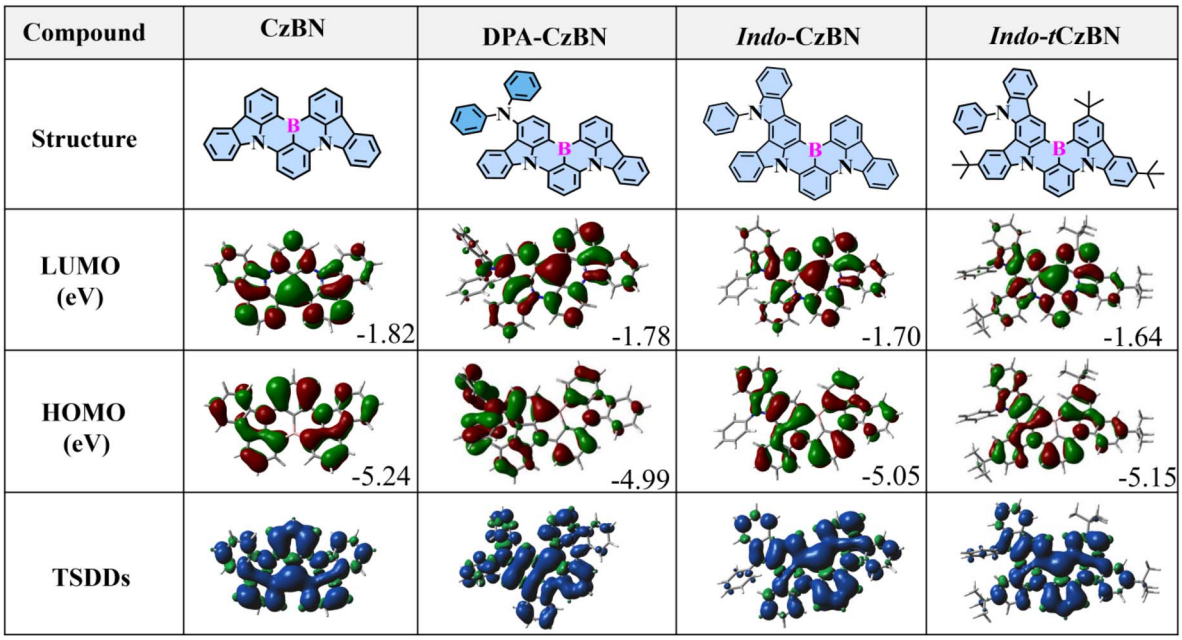

Fig. 1 Molecular structures, frontier molecular orbital (FMO) distributions and energy levels, and spin–orbital density of the T_1 state of CzBN, DPA-CzBN, Indo-CzBN, and Indo-*t*CzBN, respectively.

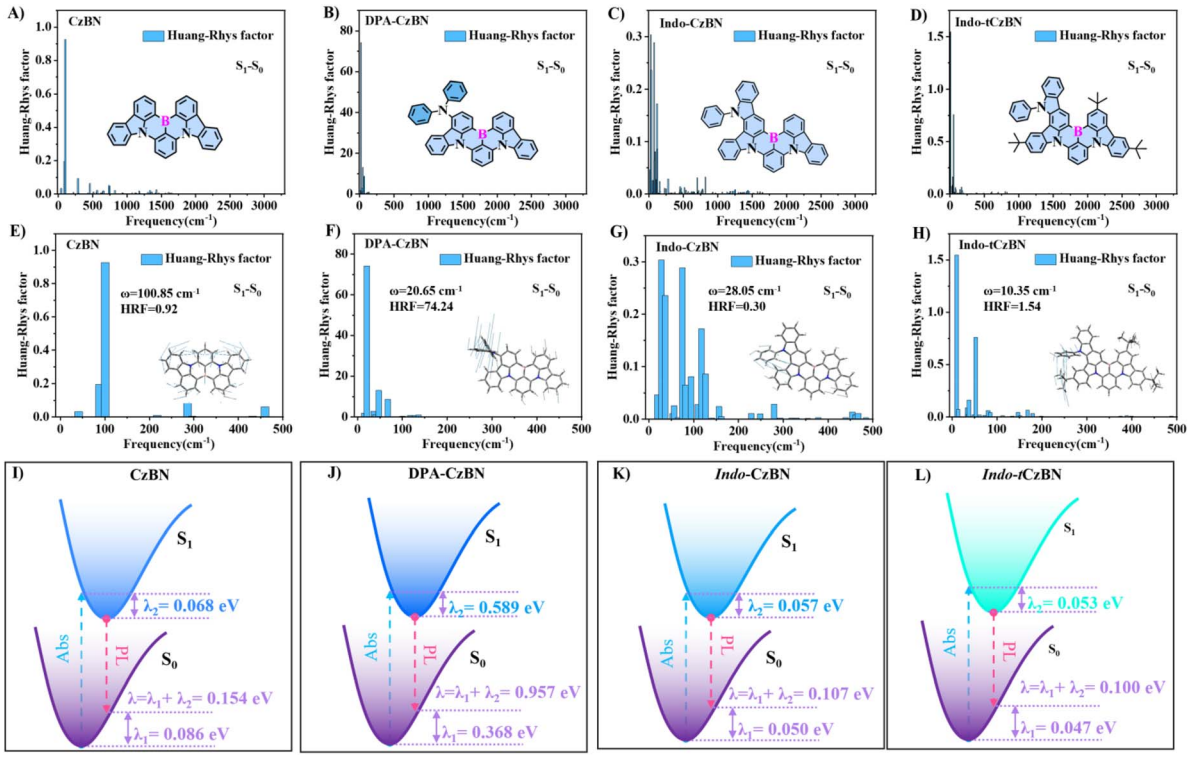

Fig. 2 Calculated Huang–Rhys (HR) factor for the $S_1 \rightarrow S_0$ transition of (A and E) CzBN, (B and F) DPA-CzBN, (C and G) Indo-CzBN, and (D and H) Indo-*t*CzBN, respectively. To facilitate the analysis, we provide two distinct frequency ranges. Reorganization energy of (I) CzBN, (J) DPA-CzBN, (K) Indo-CzBN, and (L) Indo-*t*CzBN, respectively.

carbazole group shows specific inert shielding effects on the distribution of frontier molecular orbitals (FMOs). This feature is vital for MR-TADF emitters, which typically exhibit long τ_{DF}, as it helps reduce non-radiative decay driven by the DET mechanism-dominated intermolecular interactions.

Meanwhile, time-dependent DFT (TD-DFT) calculations were also employed to comprehensively investigate the electronic properties of CzBN, DPA-CzBN, Indo-CzBN, and Indo-*t*CzBN in excited states (Fig. S3–S5). As expected, all the molecules exhibited high oscillator strength (*f*) in the S_1 state, a characteristic that traditional TADF materials lack (Fig. S3). This suggests that these molecules are likely to undergo rapid radiative decay (κ_R). On the other hand, although the NTO distributions of the T_1 states in all molecules are similar to those of the S_1 state, the NTO distributions of the T_2 and T_3 states exhibit significant differences compared to the S_1 state (Fig. S4 and S5). It has been reported that in MR-TADF materials, triplet excitons can undergo RISC *via* high-energy triplet (T_n, $n \geq 2$) states back to the S_1 state, leading to radiative emission and improved exciton utilization efficiency. In this context, the distinct NTO distributions of the T_2 and T_3 states relative to the S_1 state may substantially enhance the efficiency of triplet exciton utilization.[2d,e]

The above DFT calculations confirm that this series of materials exhibits MR properties and can produce very narrow emission. To gain deeper insight into the relationship between molecular structure and emission narrowing, we systematically computed the Huang–Rhys factor (HR), the recombination energy (λ), and the root-mean-square displacement (RMSD), thereby providing more robust theoretical support (Fig. 2 and S6). It was found that within 500–3000 cm^{-1}, the HR factor is minimal, indicating that vibrational modes associated with molecular stretching vibrations, which typically contribute to emission broadening, are significantly suppressed. In the low-frequency region (0–500 cm^{-1}), low-energy vibrational modes $\leq$300 cm^{-1}, such as scissoring/twisting vibrations, were observed. Consequently, all vibronic transitions associated with these low-energy vibrational modes are combined into a single emission peak, resulting in a narrow FWHM. We also calculated the λ_s for all molecules (Fig. 2I–L). The results showed that both Indo-CzBN and Indo-*t*CzBN had very low λ_s, indicating that the fused-PAH structure can significantly suppress vibrational relaxation in the excited state, thereby narrowing the emission spectrum and effectively reducing the Stokes shift. In contrast, DPA-CzBN showed a relatively higher λ. Further analysis of the RMSD between the S_0 and S_1 states revealed that DPA-CzBN also possesses a greater geometric structural change than CzBN, Indo-CzBN, and Indo-*t*CzBN (Fig. S6). Structural analysis suggested that conformational deformation occurs during the excited-state process. However, these deformations primarily arise from dihedral (scissoring) and torsional (twisting) vibrations below 200 cm^{-1}, which correspond to low-frequency vibrational modes and are expected to have only a minor influence on the FWHM of the emission spectra.

In dilute toluene solutions (10^{-5} M), the ultraviolet-visible (UV-vis) absorption spectra and photoluminescence (PL)

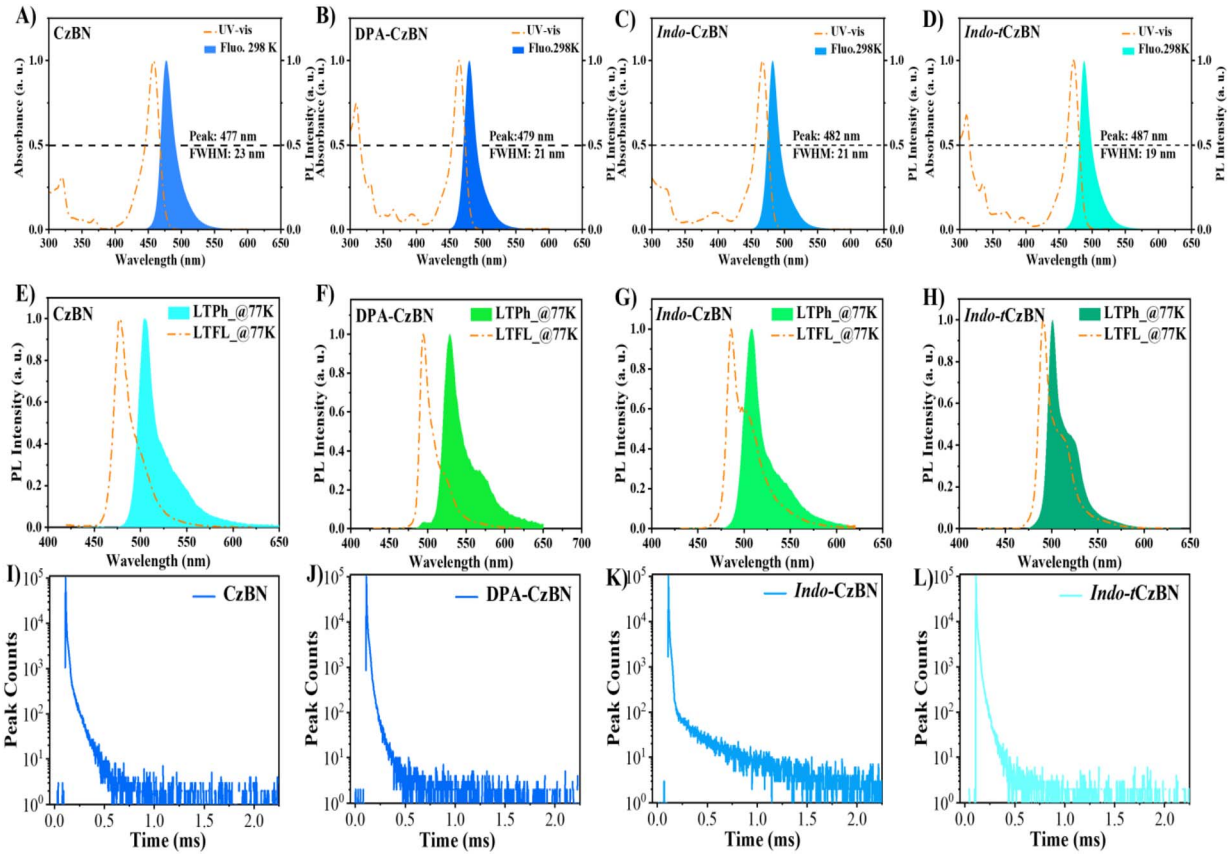

Fig. 3 Ultraviolet-visible (UV-vis) absorption and PL spectra of (A) CzBN, (B) DPA-CzBN, (C) Indo-CzBN, and (D) Indo-*t*CzBN, respectively. Low-temperature fluorescence (LTFL) and low-temperature phosphorescence (LTPh) spectra of (E) CzBN, (F) DPA-CzBN, (G) Indo-CzBN, and (H) Indo-*t*CzBN in toluene dilute solution at 77 K. Transient PL spectra of (I) CzBN, (J) DPA-CzBN, (K) Indo-CzBN, and (L) Indo-*t*CzBN, respectively, in doped films.

spectra of the four molecules were investigated. In UV-vis spectra, for all molecules within the wavelength range of 300–400 nm, a mixed absorption band exists that can be attributed to the intrinsic π–π* absorption transition and n–π* transition of these molecules. Within the range of 400–500 nm, a strong and narrow absorption band appears, originating from the short-range intramolecular charge transfer (ICT) transition caused by the MR effect induced by B/N-PAH (Table S1). In PL spectra, consistent with the reference CzBN, DPA-CzBN exhibits a smaller FWHM of 21 nm (Fig. 3 and Table S1). On the other hand, both Indo-CzBN and Indo-*t*CzBN demonstrate very narrow FWHMs, suggesting that fused-PAH strategies can excessively restrict geometrical deformation to some degree in the S_1 state. Additionally, we examined the luminescence properties of CzBN, DPA-CzBN, Indo-CzBN, and Indo-*t*CzBN in various polar solvents, known as the "solvatochromism effect" (Fig. S10 and Table S3). Compared to CzBN, DPA-CzBN, Indo-CzBN, and Indo-*t*CzBN showed narrower FWHMs in both low-polarity and high-polarity solvents, indicating a weaker solvatochromic effect. For example, in DMF, the FWHM of CzBN was as high as 31 nm, while those of Indo-CzBN and Indo-*t*CzBN were 25 nm and 26 nm (Table S2), respectively. This may be due to the more rigid, fused-PAH molecular skeleton of Indo-CzBN and Indo-*t*CzBN, which suppresses vibrational relaxation and excited-state structural rearrangements. Furthermore, the low-temperature fluorescence (LTFL) and low-temperature phosphorescence (LTPh) spectra of CzBN, DPA-CzBN, Indo-CzBN, and Indo-*t*CzBN in a toluene dilute solution at 77 K were measured to determine their energy levels of the S_1 and T_1 states (Fig. 3E–H and Table S1). Compared to CzBN, Indo-CzBN and Indo-*t*CzBN with a fused-PAH framework exhibit smaller singlet–triplet splitting energies (ΔE_{ST}). Notably, the energy difference of Indo-*t*CzBN is as low as 0.04 eV, which is highly conducive to converting triplet excitons into the S_1 state *via* RISC processes, thereby achieving efficient exciton utilization. To confirm the TADF characteristics of all the materials, we further measured their transient PL spectra in doped films (Fig. 3I–L and Table S4). All emitters exhibited double-exponential decay, indicating efficient utilization of triplet excitons in these materials. In particular, compared with CzBN, DPA-CzBN, Indo-CzBN, and Indo-*t*CzBN have shorter radiative decay lifetimes (τ_{PF} ~4 ns), resulting in higher κ_r^s values of up to $10^8\ s^{-1}$ (Table S3). Additionally, in the doped system, the PLQYs of the films based on CzBN, DPA-CzBN, Indo-CzBN, and Indo-*t*CzBN were measured (Table S3). The results reveal that, despite sharing a similar core structure, these molecules exhibit markedly different PLQY values. Notably, the PLQY of Indo-*t*CzBN (97.5%) has increased by ~20% relative to Indo-CzBN

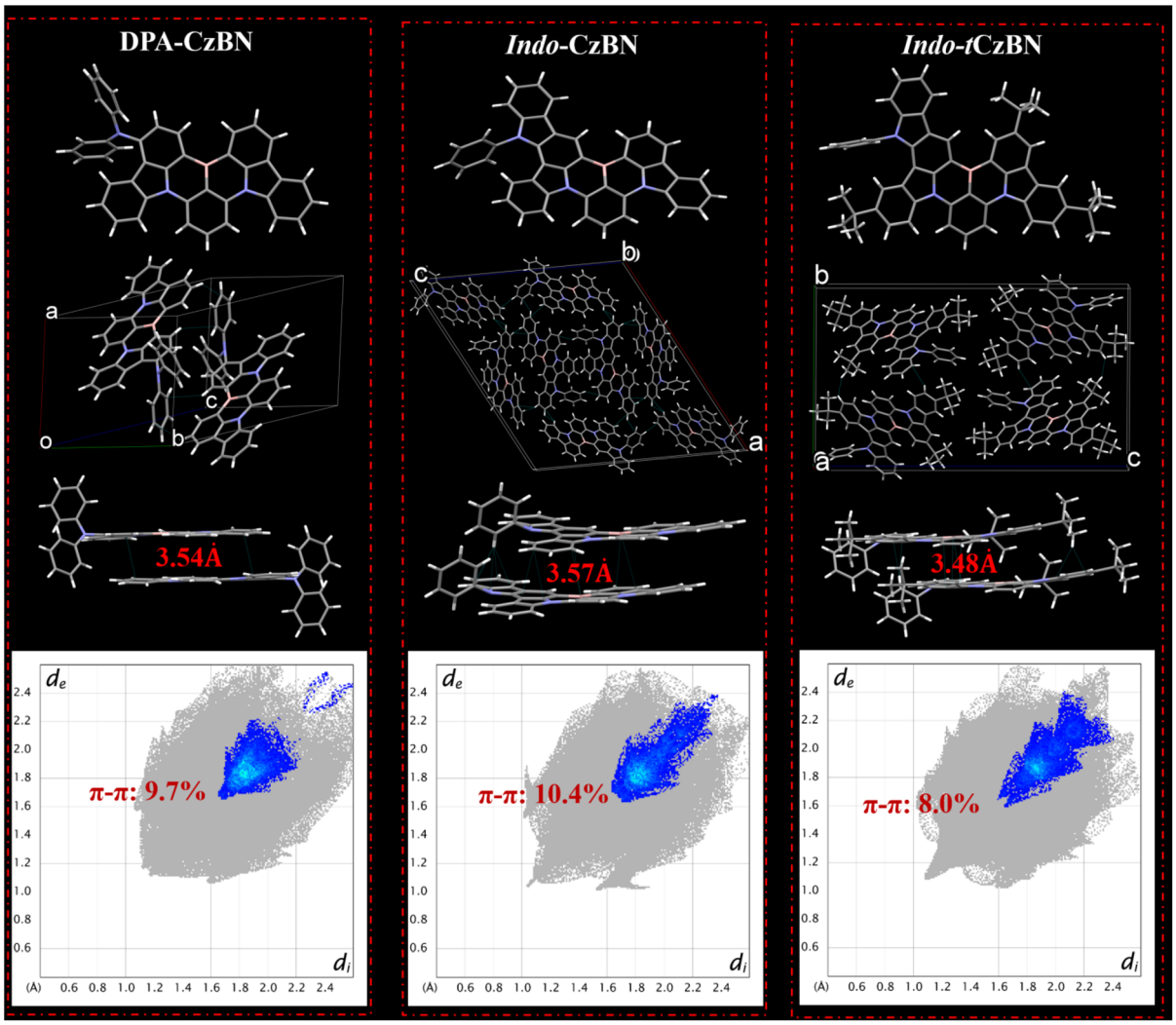

Fig. 4 Single-crystal and unit cell structures, intermolecular packing patterns with the most compact dimer structures, and the primary intermolecular π–π interactions in DPA-CzBN, Indo-CzBN, and Indo-*t*CzBN within their crystals.

(81.2%), reflecting a significant enhancement. This substantial increase indicates that the incorporation of *t*-Bu groups efficiently inhibits non-radiative decay pathways in Indo-*t*CzBN.

We successfully obtained single crystals of DPA-CzBN, Indo-CzBN, and Indo-*t*CzBN *via* the chloroform/methanol solvent diffusion method (Fig. 4 and S11–14). Interestingly, although the three emitters share similar chemical structures, their single-crystal packing patterns still differ. From the crystal cell structures of each, it is evident that, compared with DPA-CzBN, Indo-CzBN and Indo-*t*CzBN exhibit more extensive intermolecular interactions. Additionally, the most densely packed dimer structures were individually extracted from their single crystals, and the shortest intermonomer distances are 3.54 Å, 3.57 Å, and 3.48 Å, respectively, indicating that the molecular spacings among the three are comparable (Fig. 4). Furthermore, to gain deeper insights into the packing characteristics of DPA-CzBN, Indo-CzBN, and Indo-*t*CzBN, a comprehensive analysis of the primary intermolecular interactions was conducted using Hirshfeld surface analysis (Fig. 4 and S7–S9),[11] indicating that weak interactions, specifically C–H···H–C (45.8–68.2%) and C–H···π (24.3–37.2%), predominantly govern the intermolecular interactions in DPA-CzBN, Indo-CzBN, and Indo-*t*CzBN (Fig. S7–S9). More importantly, DPA-CzBN, Indo-CzBN, and Indo-*t*CzBN exhibit π–π interactions, accounting for 9.7%, 10.4%, and 8.0%, respectively. Notably, in MR-TADF materials, exciton quenching primarily occurs *via* the DET mechanism, which depends on electron exchange between bimolecules and is highly sensitive to intermolecular distance; thus, even slight changes in intermolecular interactions (*e.g.*, π–π or C–B···π) can significantly influence exciton annihilation. Specifically, in Indo-*t*CzBN, the introduction of multiple *t*-Bu groups weakens intermolecular interactions to some extent, thereby effectively reducing π–π stacking, which is anticipated to enhance both the PL and EL properties of Indo-*t*CzBN. Such a structural alteration may partially account for the higher PLQY of Indo-*t*CzBN relative to Indo-CzBN.

To evaluate the intrinsic EL properties of DPA-CzBN and Indo-*t*CzBN, non-sensitized OLEDs were first fabricated using mCPBC as the host material, which has high S_1 and T_1 energy (Fig. 5 and S15–S17). OLEDs based on CzBN and Indo-CzBN

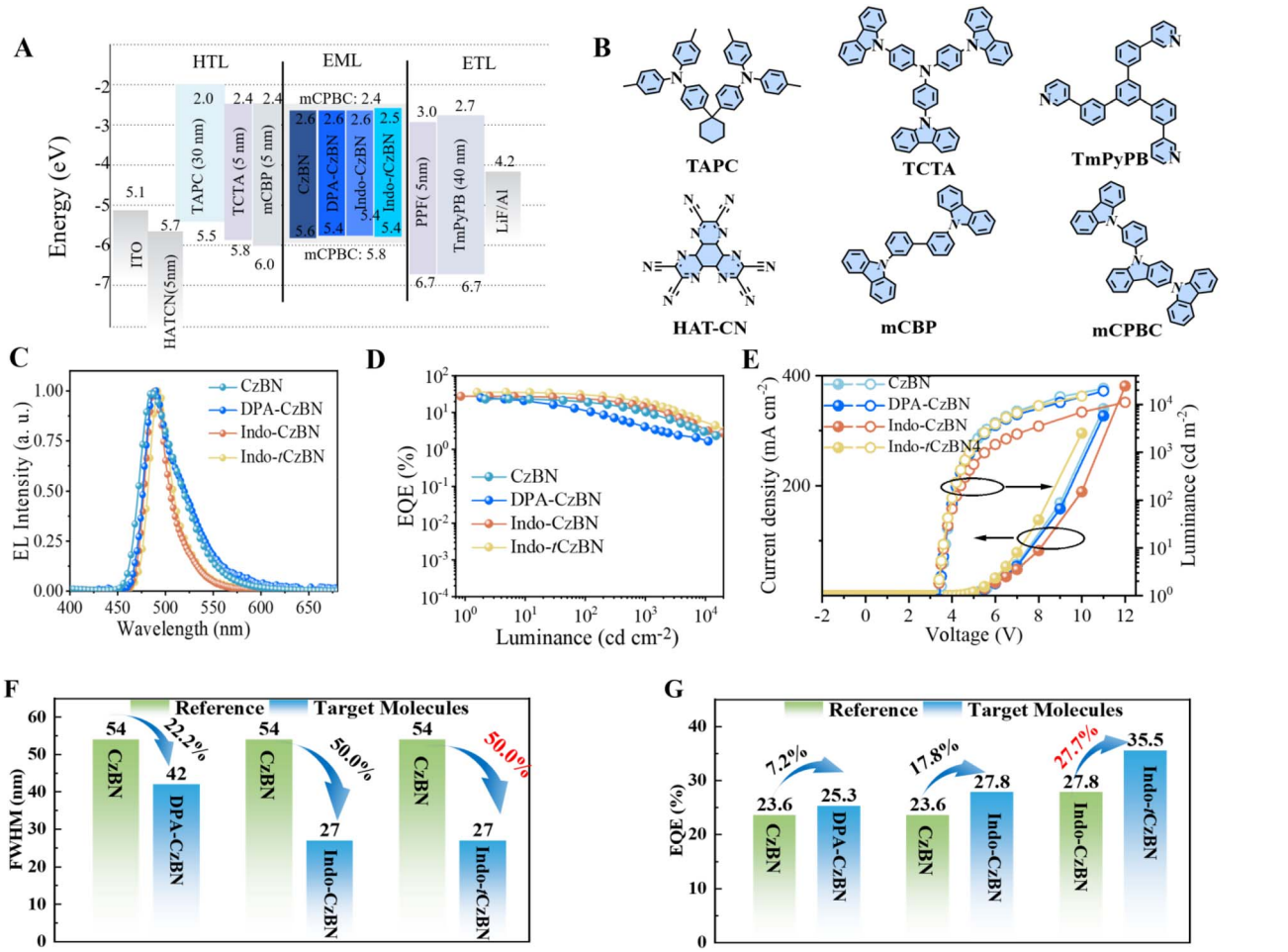

Fig. 5 (A) The device architecture and energy diagram, (B) functional layer materials used in these OLEDs, (C) EL spectra, (D) EQE–luminance curves, (E) current density–voltage–luminance curves, (F) comparison chart of FWHM values, and (G) comparison chart of EQE_{max} values of non-sensitized OLEDs based on CzBN, DPA-CzBN, Indo-CzBN, and Indo-*t*CzBN with a doping concentration of 3 wt%.

with the same device structure were also fabricated for comparison. The device structure is shown in Fig. 5A, and the materials used for the key functional layers are summarized in Fig. 5B. The HOMO and LUMO of CzBN, DPA-CzBN, Indo-CzBN, and Indo-*t*CzBNB were evaluated by cyclic voltammetry (Fig. S15). To accurately assess the EL performance of these new emitters, OLEDs were fabricated with doping concentrations of 1, 3, and 5 wt%. The experimental data for all non-sensitized

Table 1 EL performance of non-sensitized OLEDs based on CzBN, DPA-CzBN, Indo-CzBN, and Indo-*t*CzBN, respectively

Emitter	Dop. [wt%]	V_{on}[a] [V]	$CE_{max}/PE_{max}/EQE_{max}$[b] (cd A^{-1})/(lm W^{-1})/(%)	FWHM (nm)	L_{max} (cd m^{-2})	λ_{EL}[c] (nm)	CIE[d] (x, y)
CzBN	1	3.5	39.6/35.6/24.7	31	10 990	482	(0.10, 0.29)
	3	3.5	52.7/47.0/23.7	46	13 440	486	(0.13, 0.43)
	5	3.4	58.1/52.2/23.6	54	15 010	490	(0.14, 0.48)
DPA-CzBN	1	3.5	39.3/35.3/24.4	26	11 140	486	(0.09, 0.32)
	3	3.5	45.8/21.1/25.5	31	8954	488	(0.09, 0.37)
	5	3.4	47.2/43.6/25.3	42	11 160	490	(0.09, 0.40)
Indo-CzBN	1	3.7	40.5/34.2/25.6	25	17 130	484	(0.09, 0.30)
	3	3.5	56.4/49.2/27.1	27	18 460	486	(0.11, 0.41)
	5	3.4	66.9/60.9/27.8	27	19 220	490	(0.14, 0.48)
Indo-*t*CzBN	1	3.6	58.3/50.9/33.8	26	20 300	490	(0.08, 0.37)
	3	3.5	72.1/64.7/37.4	26	22 460	492	(0.08, 0.44)
	5	3.5	73.1/65.4/35.5	27	21 770	492	(0.08, 0.46)

[a] V_{on} denotes the voltage value when the luminance is 1 cd m^{-2}. [b] CE represents current efficiency, PE is power efficiency, and EQE is external quantum efficiency. [c] λ_{EL} denotes the emission peak at a current density of 5 mA cm^{-2}. [d] CIE denotes Commission Internationale de l'Eclairage.

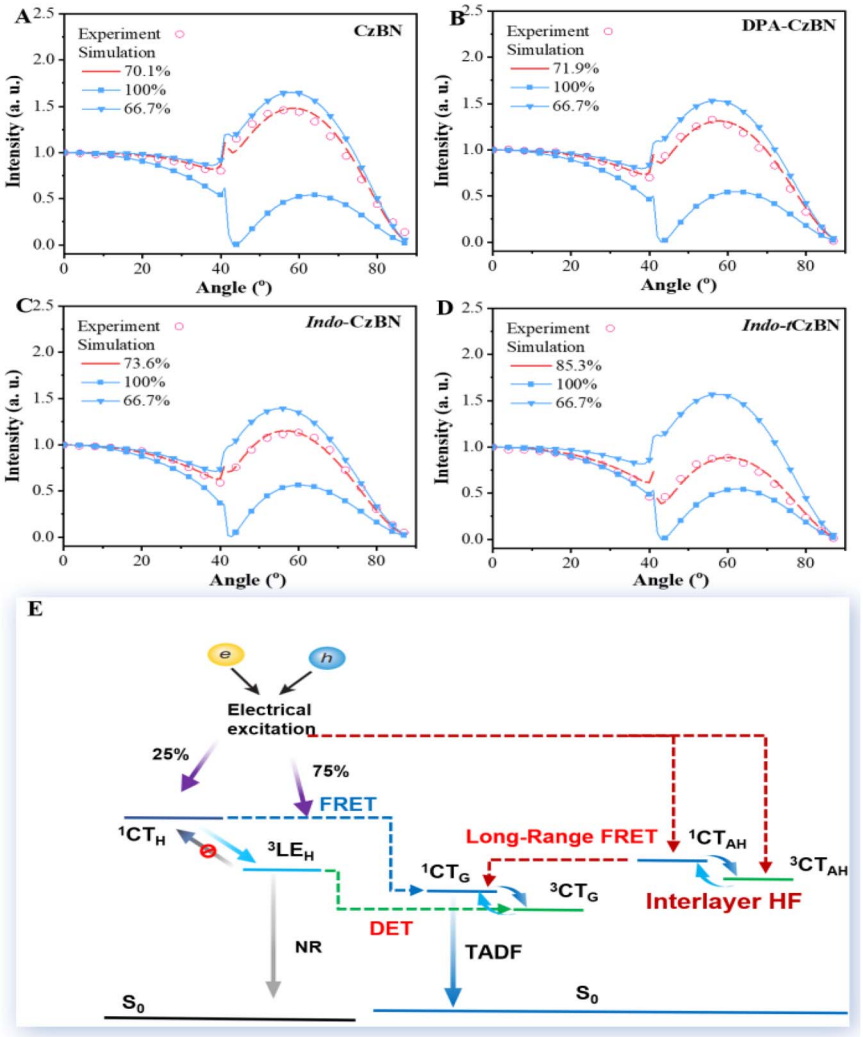

Fig. 6 The horizontal dipole orientation factor of (A) CzBN, (B) DPA-CzBN, (C) Indo-CzBN, and (D) Indo-*t*CzBN in 3 wt% doped systems. (E) Schematic diagram of the exciton dynamics process under electric excitation conditions of the interlayer hyperfluorescence (HF) strategy.

devices are summarized in Table 1. Regarding FWHM values, it is essential to note that for OLEDs based on CzBN, the FWHM is much broader than in solutions (Fig. 3, Tables S1 and S2), ranging from 31 nm (1 wt%) to 52 nm (5 wt%) (Fig. 5C, S16C, S17C, and Table 1). Similarly, non-sensitized OLEDs based on DPA-CzBN showed an increasing FWHM: at 1 wt%, it was 26 nm, rising to 42 nm at 5 wt%. Although the DPA unit partially reduced the FWHM broadening, its effect remained limited. Conversely, Indo-CzBN and Indo-*t*CzBN, which feature rigid PAH structures, exhibit a strong ability to suppress FWHM broadening in OLEDs. For instance, at a doping concentration of 3 wt%, the FWHM values of OLEDs based on Indo-CzBN and Indo-*t*CzBN were only 27 nm and 26 nm, respectively, which are 41.3% and 43.5% lower than those of devices based on CzBN (Fig. 5F and Table 1), an impressive outcome.

In terms of EQE values, at the same doping concentration (*e.g.*, 3 wt%), the peak EQE of OLEDs based on DPA-CzBN, Indo-CzBN, and Indo-*t*CzBN showed varying degrees of improvement compared to the reference molecule CzBN (Fig. 5G and Table 1). This trend aligns with changes in PLQY values of these emitters in doped films. In particular, compared with CzBN, OLEDs based on DPA-CzBN showed only a slight improvement (Fig. 5G and Table 1), indicating that DPA's effect on improving the EL performance of DPA-CzBN is relatively limited. Notably, compared with CzBN, the OLED based on Indo-*t*CzBN exhibited a 57.8% increase in efficiency (Fig. 5G and Table 1), reaching a maximum EQE of 37.5%; even compared with the device based on Indo-CzBN, its efficiency improved by 27.7%. Further analysis indicates that the high EQE of the Indo-*t*CzBN device is primarily attributable to the synchronous optimization of its internal quantum efficiency and light-extraction efficiency. The improvement in internal efficiency is attributed to the PLQY of up to 97.5% in the doped film, which is suppressed by the spatial shielding effect of *tert*-butyl, thereby inhibiting intermolecular Dexter energy transfer and non-radiative decay pathways. Notably, the OLED based on Indo-*t*CzBN has achieved synergistic optimization, achieving both a narrow FWHM and an exceptionally high EQE, ranking among the highest reported in the current literature (Table S6).[2c–e,6b,8,12]

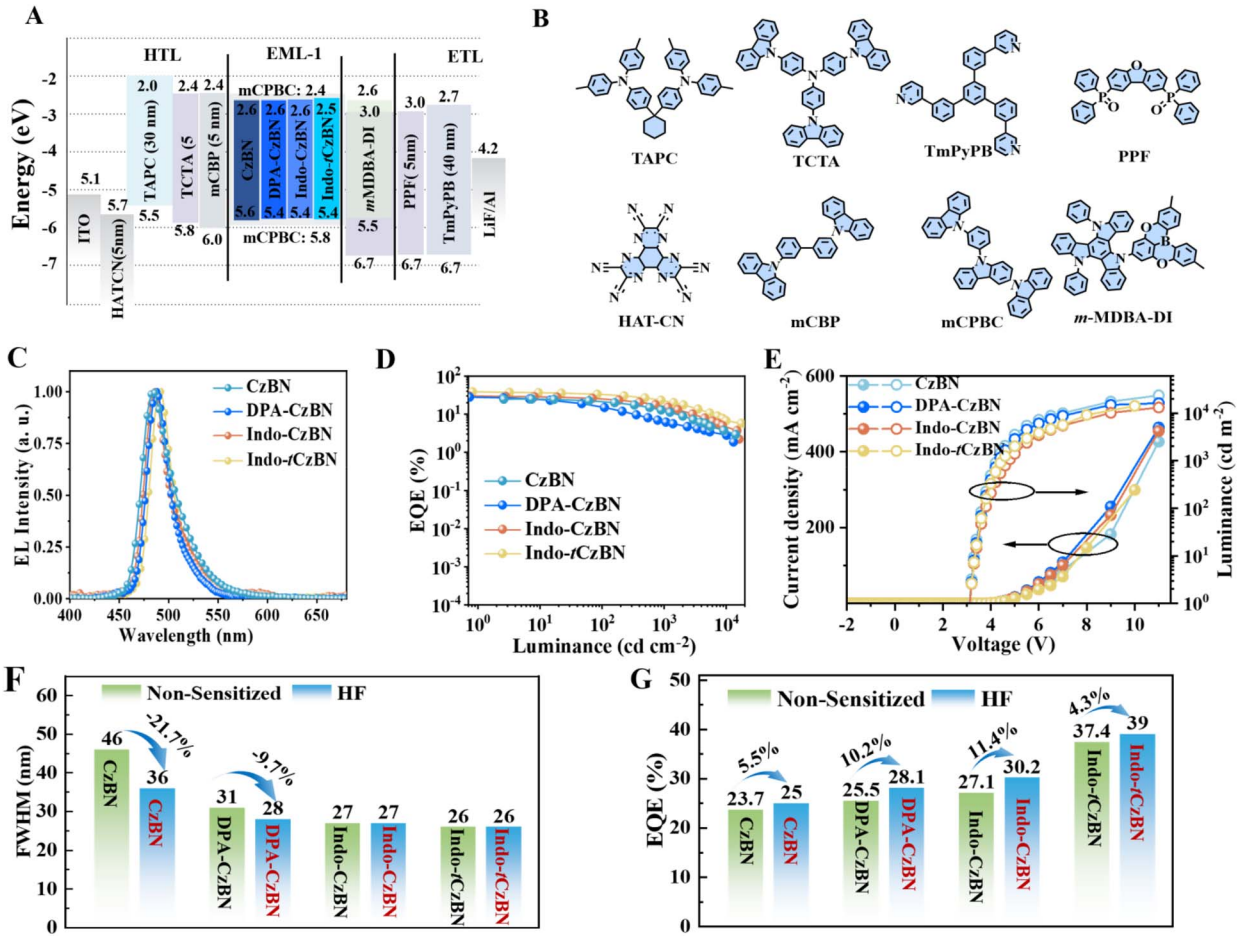

Fig. 7 (A) The device architecture and energy diagram, (B) functional layer materials, (C) EL spectra, (D) EQE-luminance curves, anf (E) current density–voltage–luminance curves of interlayer hyperfluorescence (HF) OLEDs based on CzBN, DPA-CzBN, Indo-CzBN, and Indo-*t*CzBN with a doping concentration of 3 wt%. (F) Comparison chart of FWHM values between non-sensitized and interlayer HF-OLEDs. (G) Comparison chart of EQE_{max} values between non-sensitized and interlayer HF-OLEDs. Here, the conventional TADF emitter m-MDBA-DI, known for high EL performance, was used as an assisting host for the interlayer HF.

In addition to the high EQE arising from improved PLQY, we propose that other factors contributed to enhancing the overall device efficiency. We therefore further examined the orientation characteristics of the transition dipole moment in 3 wt% CzBN-, DPA-CzBN-, Indo-CzBN-, and Indo-*t*CzBN-doped mCPBN matrices. As illustrated in Fig. 6A–D, $\Theta// = 100\%$ corresponds to a perfectly horizontal alignment, whereas $\Theta// = 67\%$ represents a completely isotropic distribution, which serves as a theoretical reference. The experimental results indicate that the doped films based on CzBN, DPA-CzBN, and Indo-CzBN exhibit only moderate orientation factors, with $\Theta//$ values of 70.1%, 71.9%, and 73.1%, respectively. Considering their PLQY values, this $\Theta//$ characteristic provides a reasonable explanation for their relatively modest EL performance. Notably, the doped film incorporating multi-*t*-Bu-modified Indo-*t*CzBN achieved a significantly higher $\Theta//$ value of 85.3%, far exceeding those of the other comparable materials. Combined with its outstanding PLQY, this highly ordered molecular orientation creates favorable conditions for achieving higher light extraction efficiency in the device. This observation reasonably accounts for the markedly superior EL performance of Indo-*t*CzBN in OLEDs compared to CzBN, DPA-CzBN, and Indo-CzBN.

Considering the different polarity requirements of MR-TADF emitters and TADF sensitizers for host materials, traditional homogeneous sensitization designs often struggle to achieve both high EL efficiency and a narrow FWHM simultaneously. The interlayer sensitization strategy addresses this issue by placing the MR-TADF emitter and the TADF sensitizer in adjacent host layers with low and high polarity, respectively (Fig. 6E). This method promotes efficient energy transfer *via* long-range Förster resonance energy transfer (FRET), thereby effectively addressing polarity mismatch and greatly enhancing exciton utilization. Thus, to fully utilize excitons and improve device performance, we introduced the conventional TADF emitter m-MDBA-DI, which exhibits high EL performance, as an assisting host material for the interlayer hyperfluorescence (interlayer HF) system (Fig. 7 and Table S5). This interlayer design not only resolves the polarity mismatch between the main materials but also accounts for the fundamental photophysical differences between MR-TADF emitters and traditional TADF sensitizers. MR-TADF materials typically exhibit high

oscillator strength but weak spin–orbit coupling, which is conducive to narrow-spectrum radiation but not to rapid RISC; by contrast, traditional TADF sensitizers generally have strong spin–orbit coupling to achieve rapid RISC but exhibit a wider emission spectrum. Spatially separating the two effectively avoids their mutual interference in the mixed layer, allowing each material to operate in its optimal physical and chemical environment. Energy is transferred *via* long-range FRET, which imposes relatively loose spectral-overlap requirements, thereby enabling efficient triplet-exciton collection while preserving the narrow-spectral characteristics of MR-TADF emitters. The device architecture is illustrated in Fig. 7A, and the key functional-layer materials are summarized in Fig. 7B. In this type of HF-OLEDs, we unexpectedly observed that the FWHM values of HF-OLEDs based on CzBN and DPA-CzBN exhibited varying degrees of reduction. Notably, the device's FWHM, based on the reference emitter CzBN, decreased by 21.7%, thereby mitigating spectral broadening induced by the host material (Fig. 7C and F). More importantly, compared with non-sensitized devices, the interlayer HF-OLEDs demonstrated further performance enhancements (Fig. 7D, G and Table S5). In particular, the HF-OLED based on Indo-*t*CzBN achieved an EQE_{max} of up to 39.0%, surpassing its original high performance (EQE ~37.4%) and ranking among the top-performing devices reported for MR-TADF material systems based on a single BN structure (Tables S5 and S6).

Conclusion

We propose a "terminal engineering" strategy to simultaneously enhance EL efficiency and reduce the FWHM of the emission spectra. By introducing flexible DPA groups into the structurally simple CzBN and insulating *t*-Bu groups into the PAH-based Indo-CzBN, two novel concept-proof MR-TADF materials, DPA-CzBN and Indo-*t*CzBN, were successfully developed. It was found that introducing DPA could only slightly narrow the FWHM of DPA-CzBN. At the same time, the indolocarbazole derivatives with PAH structures could significantly suppress the vibrational relaxation of the excited state, thereby significantly narrowing the FWHM of Indo-CzBN and Indo-*t*CzBN. As a result, the FWHM decreased from 23 nm for CzBN to 19 nm for Indo-*t*CzBN in dilute toluene solution. Further studies revealed that introducing insulating *t*-Bu groups could increase the distance between the luminescent centers of the molecules, effectively suppressing non-radiative energy loss and thereby significantly improving the optoelectric performance of Indo-*t*CzBN (PLQY ~97.5%). Notably, the introduction of *t*-Bu also considerably increased the Θ// of Indo-*t*CzBN to up to 85.3%. Owing to the synergistic effect of the high Θ// factor and high PLQY, non-sensitized and sensitized OLED devices based on Indo-*t*CzBN achieved EQE_{max} values of 37.4% and 39.0%, respectively, ranking among the highest reported for MR-TADF materials based on a single BN molecular skeleton. This study presents a new approach to developing high-efficiency, low-cost luminescent materials for ultra-high-definition displays, demonstrating broad applicability.

Author contributions

All authors contributed equally to this work and participated in discussions regarding the manuscript.

Conflicts of interest

The authors declare no conflict of interest.

Data availability

CCDC 2485480–2485482 (DPA-CzBN, Indo-CzBN and Indo-*t*CzBN) contain the supplementary crystallographic data for this paper.[13a–c]

All the data supporting the results of this study are provided as supplementary information (SI) to this article. Supplementary information: synthetic procedures, ^{1}H nuclear magnetic resonance spectra, mass spectra, thermogravimetric analysis, electrochemical data, photophysical property characterization, and complete electroluminescence performance data of organic light emitting diodes. See DOI: https://doi.org/10.1039/d5sc10069k.

Acknowledgements

This work was financially supported by the National Natural Science Foundation of China for Young Scholars (Class B) [Formerly National Science Fund for Distinguished Young Scholars] (22522512), the National Natural Science Foundation of China (22375212, U21A20331, 51773212, and 81903743), the National Natural Science Foundation of China for Young Scholars (Class C) (22505278), the Hundred Talents Program of the Chinese Academy of Sciences (Y60707WR48), the Zhejiang Province "Leading Goose" R&D Project (2024C01261), the Ningbo Key Scientific and Technological Project (2022Z124, 2022Z119, and 2022Z120) and the China Postdoctoral Science Foundation (2024M763380).

References

1 (*a*) D. Zhang, T. Huang and L. Duan, *Adv. Mater.*, 2020, **32**, e1902391; (*b*) S. H. Ko and J. Rogers, *Adv. Funct. Mater.*, 2021, **31**, 2106546; (*c*) H. Fang, J. Guo and H. Wu, *Nano Energy*, 2022, **96**, 107112; (*d*) Y. Yang, X. Guo, M. Zhu, Z. Sun, Z. Zhang, T. He and C. Lee, *Adv. Energy Mater.*, 2022, **13**, 2203040; (*e*) Y. Ding, J. Jiang, Y. Wu, Y. Zhang, J. Zhou, Y. Zhang, Q. Huang and Z. Zheng, *Chem. Rev.*, 2024, **124**, 1535–1648.

2 (*a*) X. Yang, G. Zhou and W. Y. Wong, *Chem. Soc. Rev.*, 2015, **44**, 8484–8575; (*b*) J. Jayabharathi and V. Thanikachalam, *Phys. Chem. Chem. Phys.*, 2024, **26**, 13561–13605; (*c*) H. J. Kim and T. Yasuda, *Adv. Opt. Mater.*, 2022, **10**, 2201714; (*d*) M. Mamada, M. Hayakawa, J. Ochi and T. Hatakeyama, *Chem. Soc. Rev.*, 2024, **53**, 1624–1692; (*e*) X. Wu, S. Ni, C. H. Wang, W. Zhu and P. T. Chou, *Chem. Rev.*, 2025, **125**, 6685–6752.

3 (*a*) L. Wang, Y. Jiang, J. Luo, Y. Zhou, J. Zhou, J. Wang, J. Pei and Y. Cao, *Adv. Mater.*, 2009, **21**, 4854–4858; (*b*) C. J. Chiang, A. Kimyonok, M. K. Etherington, G. C. Griffiths, V. Jankus, F. Turksoy and A. P. Monkman, *Adv. Funct. Mater.*, 2012, **23**, 739–746.

4 (*a*) K. Y. Lu, H. H. Chou, C. H. Hsieh, Y. H. Yang, H. R. Tsai, H. Y. Tsai, L. C. Hsu, C. Y. Chen, I. C. Chen and C. H. Cheng, *Adv. Mater.*, 2011, **23**, 4933–4937; (*b*) J. K. Bin, N. S. Cho and J. I. Hong, *Adv. Mater.*, 2012, **24**, 2911–2915.

5 (*a*) T. Hatakeyama, K. Shiren, K. Nakajima, S. Nomura, S. Nakatsuka, K. Kinoshita, J. Ni, Y. Ono and T. Ikuta, *Adv. Mater.*, 2016, **28**, 2777–2781; (*b*) Y. Kondo, K. Yoshiura, S. Kitera, H. Nishi, S. Oda, H. Gotoh, Y. Sasada, M. Yanai and T. Hatakeyama, *Nat. Photon.*, 2019, **13**, 678–682; (*c*) S. Oda, B. Kawakami, Y. Yamasaki, R. Matsumoto, M. Yoshioka, D. Fukushima, S. Nakatsuka and T. Hatakeyama, *J. Am. Chem. Soc.*, 2022, **144**, 106–112; (*d*) S. Oda, W. Kumano, T. Hama, R. Kawasumi, K. Yoshiura and T. Hatakeyama, *Angew. Chem., Int. Ed.*, 2020, **60**, 2882–2886; (*e*) Y. Sano, T. Shintani, M. Hayakawa, S. Oda, M. Kondo, T. Matsushita and T. Hatakeyama, *J. Am. Chem. Soc.*, 2023, **145**, 11504–11511.

6 (*a*) J. Lee, N. Aizawa, M. Numata, C. Adachi and T. Yasuda, *Adv. Mater.*, 2016, **29**, 1604856; (*b*) X. F. Luo, H. X. Ni, X. Liang, D. Yang, D. Ma, Y. X. Zheng and J. L. Zuo, *Adv. Opt. Mater.*, 2023, **11**, 2203002; (*c*) H. Mubarok, A. Amin, T. Lee, J. Jung, J. H. Lee and M. H. Lee, *Angew. Chem., Int. Ed.*, 2023, **62**, e202306879.

7 (*a*) M. Li, R. Li, Z. Li, Z. Chen, D. Liu, Z. Yang, H. Xie, K. Liu and S. J. Su, *Adv. Opt. Mater.*, 2024, **13**, 2402822; (*b*) Z. Yang, D. Liu, X. Cheng, T. Wang, Z. Li, G. X. Yang, Z. Chen, J. Hu, Y. Fu, X. Nie, Y. Ren, Y. Zeng, Y. Chen, K. Liu, M. Li and S. J. Su, *Angew. Chem., Int. Ed.*, 2025, **64**, e202423602.

8 P. Jiang, J. Miao, X. Cao, H. Xia, K. Pan, T. Hua, X. Lv, Z. Huang, Y. Zou and C. Yang, *Adv. Mater.*, 2022, **34**, e2106954.

9 (*a*) L. Wu, X. Mu, D. Liu, W. Li, D. Li, J. Zhang, C. Liu, T. Feng, Y. Wu, J. Li, S. J. Su and Z. Ge, *Angew. Chem., Int. Ed.*, 2024, e202409580; (*b*) L. Wu, C. Liu, D. Liu, D. Li, W. Li, J. Zhang, X. Mu, Z. Xin, B. Liu, H. Qi, Z. Wang, D. Liu, S. J. Su, Y. Zhou, S. Wu and Z. Ge, *Angew. Chem., Int. Ed.*, 2025, e202504723.

10 (*a*) H. Lim, H. J. Cheon, S. J. Woo, S. K. Kwon, Y. H. Kim and J. J. Kim, *Adv. Mater.*, 2020, **32**, e2004083; (*b*) T. A. Lin, T. Chatterjee, W. L. Tsai, W. K. Lee, M. J. Wu, M. Jiao, K. C. Pan, C. L. Yi, C. L. Chung, K. T. Wong and C. C. Wu, *Adv. Mater.*, 2016, **28**, 6976–6983; (*c*) W. Li, M. Li, W. Li, Z. Xu, L. Gan, K. Liu, N. Zheng, C. Ning, D. Chen, Y. C. Wu and S. J. Su, *ACS Appl. Mater. Interfaces*, 2021, **13**, 5302–5311.

11 (*a*) D. Li, D. Liu, M. Li, Q. Liu, W. Liu, W. Li, S. J. Su and X. Jiang, *Chem. Sci.*, 2025, **16**, 18332–18340; (*b*) C. E. Galvez, O. E. Piro, G. A. Echeverría, K. Vignesh, S. Thamotharan, M. d. H. Loandos and D. M. Gil, *CrystEngComm*, 2025, **27**, 3806–3822.

12 (*a*) Y. K. Qu, D. Y. Zhou, F. C. Kong, Q. Zheng, X. Tang, Y. H. Zhu, C. C. Huang, Z. Q. Feng, J. Fan, C. Adachi, L. S. Liao and Z. Q. Jiang, *Angew. Chem., Int. Ed.*, 2022, **61**, e202201886; (*b*) Y. Wang, K. Di, Y. Duan, R. Guo, L. Lian, W. Zhang and L. Wang, *Chem. Eng. J.*, 2022, **431**, 133221; (*c*) Y. Zhang, J. Wei, D. Zhang, C. Yin, G. Li, Z. Liu, X. Jia, J. Qiao and L. Duan, *Angew. Chem., Int. Ed.*, 2022, **61**, e202113206; (*d*) E. Ravindran, H. E. Baek, H. W. Son, J. H. Park, Y. H. Kim and M. C. Suh, *Adv. Funct. Mater.*, 2023, **33**, 2213461; (*e*) Q. Wang, Y. Xu, T. Yang, J. Xue and Y. Wang, *Adv. Mater.*, 2023, **35**, e2205166; (*f*) H. X. Ni, J. Z. Zhu, J. J. Hu, L. Yuan, X. J. Liao, S. Xing and Y. X. Zheng, *Adv. Opt. Mater.*, 2024, **12**, 2401033; (*g*) L. Xing, J. Wang, W.-C. Chen, B. Liu, G. Chen, X. Wang, J.-H. Tan, S. S. Chen, J.-X. Chen, S. Ji, Z. Zhao, M.-C. Tang and Y. Huo, *Nat. Commun.*, 2024, **15**, 6175; (*h*) Y. K. Chen, J. Lei, Y. C. Chao, Y. C. Kung, W. Y. Hung, L. Y. Hsu and T. L. Wu, *Mater. Horiz.*, 2025, **12**, 9737–9748; (*i*) C. Jiang, Y. Nie, C. Cao, X. Song, J. Liang, X. Zhuang, Z. Li, B. Liang and Y. Wang, *Adv. Sci.*, 2025, e12796; (*j*) M. Tirupati, J. H. Ham, S. Muruganantham, S. C. Cha, Y. H. Jung and J. H. Kwon, *Angew. Chem., Int. Ed.*, 2025, **64**, e202510190.

13 (*a*) CCDC 2485480: Experimental Crystal Structure Determination, 2026, DOI: 10.5517/ccdc.csd.cc2pfbs8.; (*b*) CCDC 2485481: Experimental Crystal Structure Determination, 2026, DOI: 10.5517/ccdc.csd.cc2pfbt9; (*c*) CCDC 2485482: Experimental Crystal Structure Determination, 2026, DOI: 10.5517/ccdc.csd.cc2pfbvb.